

The Fallacy of Drifting Snow

Edgar L Andreas

Received: 4 February 2011 / Accepted: 21 July 2011 / Published online: 28 August 2011
© Springer Science+Business Media B.V. 2011

Abstract A common parametrization over snow-covered surfaces that are undergoing sal-tation is that the aerodynamic roughness length for wind speed (z_0) scales as $\alpha u_*^2/g$, where u_* is the friction velocity, g is the acceleration of gravity, and α is an empirical constant. Data analyses seem to support this scaling: many published plots of z_0 measured over snow demonstrate proportionality to u_*^2 . In fact, I show similar plots here that are based on two large eddy-covariance datasets: one collected over snow-covered Arctic sea ice; another collected over snow-covered Antarctic sea ice. But in these and in most such plots from the literature, the independent variable, u_* , was used to compute z_0 in the first place; the plots thus suffer from fictitious correlation that causes z_0 to unavoidably increase with u_* without any intervening physics. For these two datasets, when I plot z_0 against u_* derived from a bulk flux algorithm—and thus minimize the fictitious correlation— z_0 is independent of u_* in the drifting snow region, $u_* \geq 0.30 \text{ m s}^{-1}$. I conclude that the relation $z_0 = \alpha u_*^2/g$ when snow is drifting is a fallacy fostered by analyses that suffer from fictitious correlation.

Keywords Bulk turbulent flux algorithm · Drag coefficient · Fictitious correlation · Ice Station Weddell · Roughness length · Saltation · Sea ice · SHEBA · Snow · Turbulence measurements

1 Introduction

Once Owen (1964) proposed that the height of the saltation layer over a mobile surface, such as sand or snow, sets the aerodynamic roughness length (z_0), many snow scientists embraced this parametrization. Briefly, Owen's argument requires

$$z_0 = \alpha \frac{u_*^2}{g}, \quad (1)$$

where u_* is the friction velocity, g is the acceleration of gravity, and α is a constant.

Edgar L Andreas (✉)
NorthWest Research Associates, Inc. (Seattle Division), 25 Eagle Ridge, Lebanon,
New Hampshire 03766-1900, USA
e-mail: eandreas@nwra.com

Earlier, [Charnock \(1955\)](#) had used dimensional analysis and measurements of the vertical wind speed profile over a natural water body to obtain the same result empirically. When [Eq. 1](#) is applied to the aerodynamic roughness of water surfaces, it is referred to as the Charnock relation.

[Chamberlain \(1983\)](#) subsequently argued that (1), with a single α value of about 0.016, can be applied equally well over sand, snow, and the sea (cf. [Wieringa 1993](#)). Many flux parametrizations over both the ocean and snow-covered terrain therefore use (1) to parametrize z_0 .

Values of the constant α obtained over the ocean generally fall in the range 0.01–0.02 (e.g., [Smith 1988](#); [Fairall et al. 1996](#); [Johnson et al. 1998](#); [Bonekamp et al. 2002](#)). Some values of α measured over surfaces with drifting snow are also in this range and therefore seem to support [Chamberlain's \(1983\)](#) synthesis. For example, [Kind \(1976\)](#) found $\alpha = 0.010$, [Tabler \(1980\)](#) suggested $\alpha = 0.013$, and [Joffre \(1982\)](#) obtained approximately $\alpha = 0.015$. But, in general, the value of α over snow-covered surfaces seems much more variable than over the ocean. [Pomeroy and Gray \(1990\)](#) measured $\alpha = 0.06$ for snow-covered ground; [König \(1985\)](#) reported $\alpha = 0.006$ for an Antarctic ice shelf; [Andreas and Claffey \(1995\)](#) obtained $\alpha = 0.097$ over Antarctic sea ice; and [Liston and Sturm \(1998\)](#) used $\alpha = 0.06$ in their model for drifting snow over complex terrain. Finally, [Schmidt's \(1986\)](#) data, collected over a frozen, snow-covered lake in Wyoming, did not fit the dependence suggested in (1).

Because of the variety of α values obtained over saltating surfaces, [Raupach \(1991\)](#) and [Andreas and Claffey \(1995\)](#) suggested that [Eq. 1](#) is not strictly appropriate for solid surfaces with mobile roughness elements on top of them. Such surfaces are not like the ocean, whose surface is perfectly planar in the absence of wind. Rather, for snow-covered surfaces, the underlying topography likely dictates the general range of α ; it is thus not a universal constant (cf. [Doorschot et al. 2004](#)). [Andreas \(2011\)](#) provides more detail on how z_0 parametrizations over snow-covered surfaces need to be site specific.

Another issue arises, however, in validating [Eq. 1](#) with data. As I will explain shortly, most experimental evaluations of z_0 on the left-hand side of [Eq. 1](#) require the same friction velocity, u_* , that appears on the right-hand side of (1). Random measurement errors in u_* are thus well correlated with the measurement errors in z_0 . Consequently, plots of z_0 versus u_* have built-in correlation—termed fictitious correlation here—that naturally causes z_0 to increase with u_* , as (1) predicts. I believe that this fictitious correlation—not any real physical basis—explains why (1) has endured.

In this paper, I treat this issue of fictitious correlation in parametrizations of z_0 over snow-covered surfaces, and I explain mathematically how typical data analyses automatically require measured z_0 values to increase with measured u_* values. I then illustrate this effect with two large datasets collected over snow-covered sea ice: one from the Arctic (from SHEBA, the experiment to study the Surface Heat Budget of the Arctic Ocean), and one from the Antarctic (data from Ice Station Weddell). Finally, I demonstrate the correct approach to evaluating whether z_0 depends on u_* . When z_0 is evaluated from measured u_* values but plotted against the u_* values obtained from a bulk flux algorithm (a process that minimizes fictitious correlation), z_0 is independent of this bulk u_* in the drifting snow region ($u_* \geq 0.3 \text{ m s}^{-1}$), contrary to what (1) predicts. I thus conclude that (1) is a fallacious result made plausible by flawed data analyses.

2 Bulk Flux Algorithm

A key use for parametrizations of z_0 is in bulk turbulent flux algorithms. Such algorithms (cf. [Fairall et al. 1996, 2003](#)) are used to estimate the turbulent surface fluxes of momentum

(τ , also called the surface stress) and sensible (H_s) and latent (H_L) heat in analyses and models. In fact, almost all numerical weather and climate models couple the atmosphere to the underlying surface with such bulk flux algorithms (Wyngaard 2010, p. 223).

One of the goals of SHEBA was to develop bulk flux algorithms for winter and summer sea ice (Andreas et al. 1999; Uttal et al. 2002). I later invoke the winter algorithm. Because Andreas et al. (2010a,b) give full details of both SHEBA bulk turbulent flux algorithms, I describe only the basic equations here.

The main equations are based on Monin–Obukhov similarity theory and take the forms (e.g., Garratt 1992, p. 52ff.)

$$\tau \equiv \rho u_*^2 = \rho C_{Dr} S_r^2, \tag{2a}$$

$$H_s = \rho c_p C_{Hr} S_r (\Theta_s - \Theta_r), \tag{2b}$$

$$H_L = \rho L_s C_{Er} S_r (Q_s - Q_r). \tag{2c}$$

Here, ρ is the air density; c_p is the specific heat of air at constant pressure; L_s is the latent heat of sublimation; S_r is an effective wind speed at reference height r ; Θ_r and Q_r are the potential temperature and specific humidity, respectively, at height r ; and Θ_s and Q_s are the temperature and specific humidity at the surface. Because the surface is snow or ice, we evaluate Q_s as the saturation value at temperature Θ_s . Equation 2a also defines the friction velocity, u_* .

The essence of any bulk flux algorithm is how it evaluates the transfer coefficients for momentum, sensible heat, and latent heat appropriate for reference height r : respectively, C_{Dr} , C_{Hr} , and C_{Er} in Eq. 2. These derive from Monin–Obukhov similarity theory and formally are

$$C_{Dr} = \frac{k^2}{[\ln(r/z_0) - \psi_m(r/L)]^2}, \tag{3a}$$

$$C_{Hr} = \frac{k^2}{[\ln(r/z_0) - \psi_m(r/L)] [\ln(r/z_T) - \psi_h(r/L)]}, \tag{3b}$$

$$C_{Er} = \frac{k^2}{[\ln(r/z_0) - \psi_m(r/L)] [\ln(r/z_Q) - \psi_h(r/L)]}. \tag{3c}$$

In these equations, $k(= 0.40)$ is the von Kármán constant, and ψ_m and ψ_h are empirical functions of the Obukhov length

$$L = -\frac{\bar{\Theta}}{kg} \left(\frac{u_*^3}{(H_s/\rho c_p) + \frac{0.61\bar{\Theta}}{1+0.61\bar{Q}} (H_L/\rho L_s)} \right), \tag{4}$$

where, g is, again, the acceleration of gravity, and $\bar{\Theta}$ and \bar{Q} are surface-layer averages of the air temperature and specific humidity.

Andreas et al. (2010a,b; cf. Fairall et al. 1996, 2003; Andreas et al. 2008) explain that S_r in (2) is not just the measured or modelled wind speed but also includes a parametrization for gustiness. Andreas et al. also describe how the SHEBA algorithms parametrize ψ_m and ψ_h and the roughness lengths z_0 , z_T , z_Q . As with most bulk flux algorithms, (2)–(4) are coupled through the stability parameter $\zeta \equiv r/L$ and therefore must be solved iteratively.

3 Data

Ice Station Weddell drifted from early February through early June 1992 in the western Weddell Sea, running parallel to the track of Shackleton's *Endurance*. [Andreas and Claffey \(1995\)](#) and [Andreas et al. \(2004, 2005\)](#) give full details of the mean and turbulence data collected on Ice Station Weddell.

Briefly, the turbulence data relevant to my analysis derive from a sonic anemometer/thermometer and a Lyman-alpha hygrometer mounted on a tower at a height of 4.65 m and sampled at 10 Hz. The turbulent fluxes were averaged hourly and calculated as covariances, i.e.

$$\tau = -\rho \overline{uw}, \quad (5a)$$

$$H_s = \rho c_p \overline{w\theta}, \quad (5b)$$

$$H_L = \rho L_s \overline{wq}, \quad (5c)$$

where, u , w , θ , and q are turbulent fluctuations in longitudinal velocity, vertical velocity, temperature, and specific humidity, while the overbar indicates an hour of averaging.

We performed the usual coordinate rotations to align \overline{uw} with the mean wind direction and made a correction to H_L to account for the possibility of a non-zero vertical velocity ([Webb et al. 1980](#); [Fuehrer and Friehe 2002](#)). The turbulence measurements ran continuously from late February through late May 1992; we excluded data, though, when the airflow was disturbed by structures on Ice Station Weddell. The surface at Ice Station Weddell was compact, second-year sea ice with a snow cover typically 0.4–0.5 m deep.

The SHEBA ice camp drifted in the Beaufort Gyre from early October 1997 until early October 1998. The Atmospheric Surface Flux Group maintained a site in the main camp built around a 20-m tower that was instrumented at five levels with sonic anemometer/thermometers and thus measured τ and H_s at each level. We also maintained three to four remote sites instrumented with Flux-PAM (portable automated mesonet) stations ([Militzer et al. 1995](#); [Horst et al. 1997](#)). I use data from the Flux-PAM site called Baltimore here as a representative of the other SHEBA remote sites and because its one-level flux measurements are comparable to the measurements on Ice Station Weddell. [Persson et al. \(2002\)](#), [Grachev et al. \(2005, 2007\)](#), [Brunke et al. \(2006\)](#), and [Andreas et al. \(2006, 2010a,b\)](#) describe the SHEBA measurements in detail.

As brief background, the Flux-PAM stations measured τ and H_s hourly with a sonic anemometer/thermometer at a height that ranged from 2.3 to 3.5 m above the surface. There were no latent heat flux measurements at any of the PAM sites. Processing was as eddy covariances, as on Ice Station Weddell.

[Andreas et al. \(2010a,b\)](#); cf. [Brunke et al. 2006](#)) divided the SHEBA year into just two aerodynamic seasons, winter and summer, on the basis of ice conditions. In "winter," the sea ice was compact and continuously snow-covered, and the snow was dry enough to drift and blow. In "summer," the snow became too wet and sticky to drift and eventually disappeared entirely at the SHEBA camp to expose bare sea ice. Here, I focus on the SHEBA winter data because only this period includes episodes of drifting snow, and the data should also be comparable to the data from the entire Ice Station Weddell deployment. During SHEBA, winter ran from the beginning of the measurements in late October 1997 through to 14 May 1998. It resumed on 15 September 1998 and continued through to the end of September, when we began closing the SHEBA camp.

From the SHEBA and Ice Station Weddell data, z_0 can be evaluated from (2a) and (3a) as

$$z_0 = r \exp \left\{ - \left[k C_{Dr}^{-1/2} + \psi_m(\zeta) \right] \right\}, \quad (6)$$

where z_0 and r have units of metres. All quantities on the right here were measured or otherwise known. In particular, for ψ_m , I used the function from Paulson (1970) in unstable stratification and the function from Grachev et al. (2007) in stable stratification.

I screened the resulting hourly values and discarded four Ice Station Weddell cases and 153 Baltimore cases for which $z_0 \geq 0.1\text{m}$. Computed values of z_0 this large over compact, snow-covered ice are obviously erroneous (e.g., Banke et al. 1980; Overland 1985; Guest and Davidson 1991; Andreas 1995). This screening retained 866 Ice Station Weddell cases and 1470 Baltimore cases for use here. The majority of the discarded Baltimore cases occurred early in the SHEBA deployment before we had solved the problem of sensor riming.

After finding z_0 from Eq. 6, I could also calculate the drag coefficient for neutral stability at a standard reference height of 10 m from (3a) as

$$C_{DN10} = \left[\frac{k}{\ln(10/z_0)} \right]^2, \quad (7)$$

where C_{DN10} and z_0 are interchangeable quantities for characterizing the aerodynamic properties of a surface.

4 Drifting Snow Threshold

The friction velocity at which snow in extensive fields begins to drift ($u_{*,t}$) is typically about 0.3 m s^{-1} . As representative examples, Schmidt (1986) reported $u_{*,t}$ values from 0.20 to 0.51 m s^{-1} in nine cases over snow-covered Diamond Lake in Wyoming; in seven of the nine cases, $u_{*,t}$ was between 0.20 and 0.35 m s^{-1} . Mann et al. (2000) obtained $u_{*,t}$ values between 0.21 and 0.36 m s^{-1} at Halley, Antarctic, and suggested that $u_{*,t}$ is less at the end of a drifting snow event than at the beginning. These difference, however, are smaller than the uncertainty in their u_* measurements. At the Weissfluhjoch above Davos, Switzerland, Doorschot et al. (2004) made eight measurements of $u_{*,t}$. Values ranged from 0.21 to 0.69 m s^{-1} , with five values between 0.21 and 0.42 m s^{-1} . Finally, from 10 measurement runs in a wind tunnel with a snow surface, Clifton et al. (2006) concluded that “the whole data series does suggest a threshold at $u_{*,t} \approx 0.3\text{ m s}^{-1}$.”

Our observations on Ice Station Weddell and at SHEBA similarly imply that the threshold friction velocity for snow on sea ice to begin drifting is about 0.3 m s^{-1} . Figure 1 shows visual observation of drifting and blowing snow made on Ice Station Weddell and our corresponding measurements of the friction velocity. Clearly, the threshold for drifting snow was in the u_* range $0.25\text{--}0.35\text{ m s}^{-1}$.

During SHEBA, we did not have comparable visual observations of drifting and blowing snow, but a Scintec scintillometer (e.g., De Bruin et al. 2002; Andreas et al. 2003) deployed in the main camp near our 20-m tower provided serendipitous information on drifting snow. The Scintec scintillometer measured the refractive index structure parameter, C_n^2 , by propagating laser light of $0.685\text{-}\mu\text{m}$ wavelength over a path of 350 m at a height of 2.88 m during its SHEBA winter deployment and over a path of 300 m at a height of 2.60 m during its summer deployment.

Because Scintec scintillometers are usually used over land surfaces, their computer controller has built-in software to screen propagation signals for non-turbulent disturbances caused, for example, by insects crossing the laser beam. If too many of these disturbances occur during an averaging period, the system flags the C_n^2 data as low quality. During our SHEBA deployment, the system similarly identified drifting snow, falling snow, rain, drizzle,

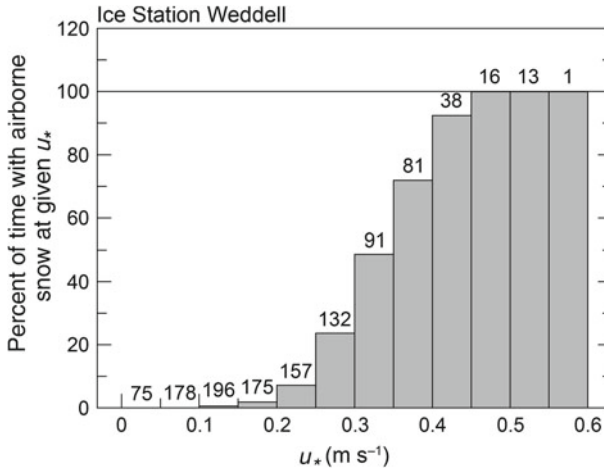


Fig. 1 Observations on Ice Station Weddell of the occurrence of drifting and blowing snow as a function of the measured friction velocity, u_* . The chart shows the percentage of observations within a u_* bin for which we observed drifting and blowing snow. The number above each bar is a count of the observation periods for which u_* was in that interval. (Observation frequency varied but was typically eight times per day.)

and fog as insect disturbances and flagged periods with these events as poor C_n^2 data. In effect, the scintillometer is a drifting snow detector.

Figure 2 compares our scintillometer observations of C_n^2 with simultaneous measurements of u_* on the nearby SHEBA 20-m tower. Both variables were averaged hourly. If, during an hour, at least 25% of the C_n^2 observations passed quality controls for insect disturbances, the hourly value are judged as good. Figure 2 shows the percentage of good C_n^2 data recorded in u_* bins that are 0.05 m s^{-1} wide during both summer and winter. Recall, by definition, that a main feature of the winter period is the potential for drifting and blowing snow; in summer, the snow was too wet and sticky to drift and eventually melted away.

In summer, the distribution of good C_n^2 data is fairly uniform with u_* : the data are good about 50% of the time. Snow squalls, drizzle, and fog probably explain the instances when the summer C_n^2 measurements failed to pass quality controls.

In winter, 50–70% of the C_n^2 values were likewise judged good when u_* was less than 0.20 m s^{-1} . Falling snow and frequent diamond dust explain the cases of poor data in this winter set. But also in winter, the cases of good C_n^2 data fell rapidly when u_* was above 0.25 m s^{-1} ; and no C_n^2 values passed the quality controls for insect disturbance when u_* was above 0.40 m s^{-1} . The fact that the summer C_n^2 data do not show this degradation with increasing friction velocity implies that other wind-dependent phenomena, such as instrument vibrations, cannot explain the winter loss of C_n^2 data. This behaviour in the winter scintillometer data must be the signature of drifting and blowing snow. And, as on Ice Station Weddell and in many other datasets, the threshold friction velocity for drifting snow during SHEBA was in the range $0.25\text{--}0.40 \text{ m s}^{-1}$.

5 Fictitious Correlation in $z_0\text{--}u_*$ Plots

Equation 1 is a standard expression for parametrizing the roughness length z_0 over any snow-covered surface (e.g., Radok 1968; Kind 1976; Tabler 1980; Male 1980; Pomeroy and Gray

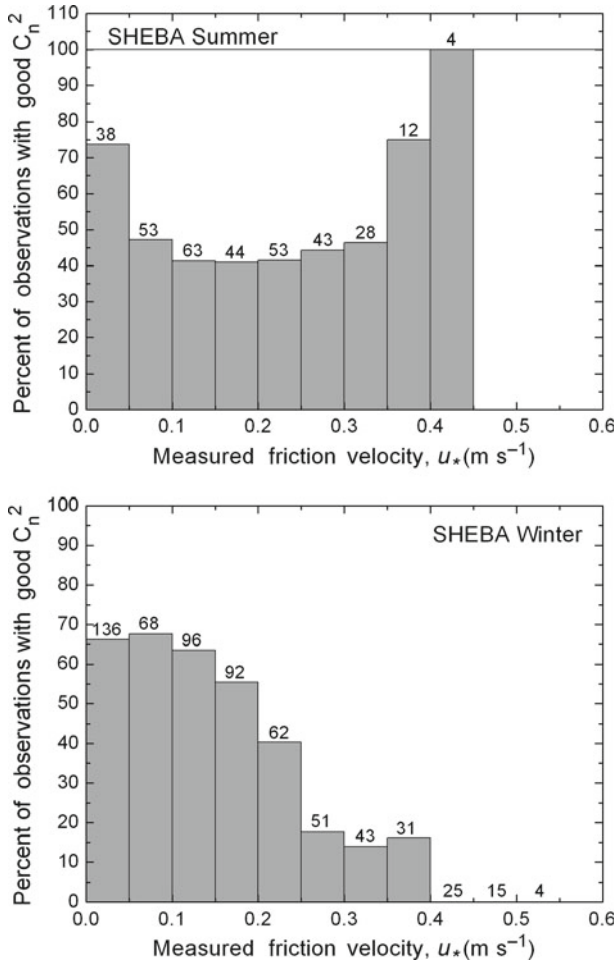


Fig. 2 SHEBA scintillometer observations of the refractive index structure parameter, C_n^2 , for both winter and summer deployments are sorted into bins in the friction velocity, u_* , as measured on the SHEBA Atmospheric Surface Flux Group’s 20-m tower. The vertical axes show the percentage of “good” C_n^2 values observed in each u_* bin. Good C_n^2 values are those that passed the built-in software screening whose purpose was, primarily, to detect propagation disturbances by insects. The number above each bar shows the hours of data (i.e., number of simultaneous C_n^2 and u_* observations) in that u_* interval

1990; Pomeroy et al. 1993; Déry and Taylor 1996; Liston and Sturm 1998; Andreas et al. 2005; King et al. 2008). For the purpose of trying to better understand how to parametrize z_0 and, therefore, to obtain u_* for snow-covered sea ice (cf. Andreas 2011), I revisit Eq. 1. I believe that most experimental validations of it suffered from fictitious correlation (e.g., Andreas et al. 2010b).

Figure 3 shows typical plots that attempt to relate z_0 to u_* (cf. Joffe 1982; Pomeroy and Gray 1990; Bintanja and Van den Broeke 1995; Brunke et al. 2006). The data come from both Ice Station Weddell and the SHEBA Flux-PAM site called Baltimore. The z_0 values clearly tend to increase throughout the u_* range; the increase is most pronounced for small u_* in the region well below the drifting snow threshold (Figs. 1, 2). Both panels in Fig. 3 also show z_0 increasing with u_* above the saltation threshold of about $u_{*,t} = 0.30 \text{ m s}^{-1}$.

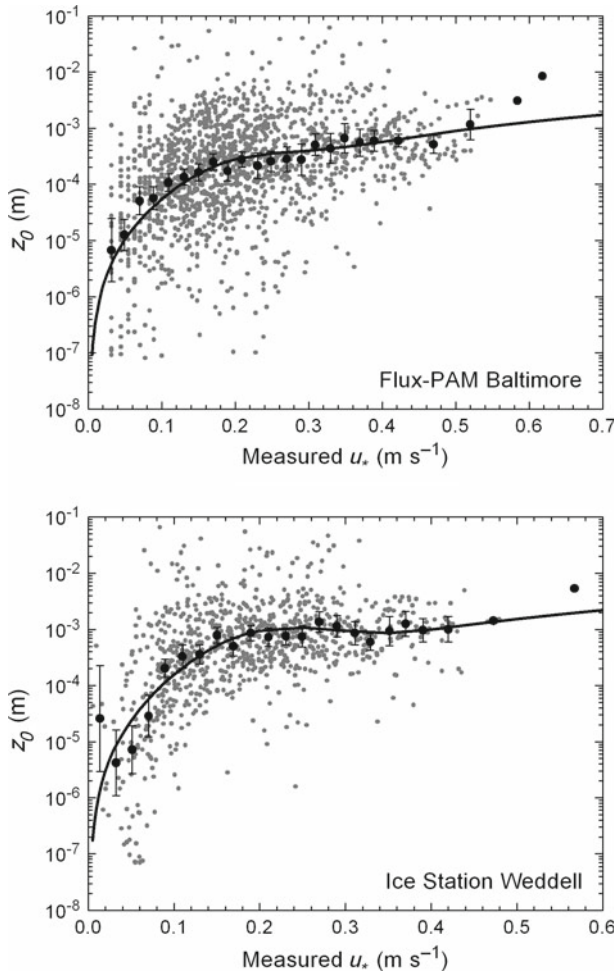


Fig. 3 Hourly measurements of the aerodynamic roughness length z_0 from Eq. 6 made over winter sea ice (gray circles) are plotted against measured values of the friction velocity, u_* . The data come from the SHEBA Flux-PAM site named Baltimore and from Ice Station Weddell. The black circles are geometric mean values of z_0 in u_* bins that are mostly 0.02 m s^{-1} wide; the error bars show ± 2 times the standard deviation in the geometric mean. Equation 8 gives the expression for the solid curves

Taking guidance from Andreas et al. (2005), I fitted similar functions to both panels in Fig. 3, viz.

$$z_0 = \frac{\alpha u_*^2}{g} \left\{ F \exp \left[- \left(\frac{u_* - 0.18}{0.10} \right)^2 \right] + 1 \right\}. \tag{8}$$

In the Baltimore panel in Fig. 3, $\alpha = 0.035$ and $F = 1$; in the Ice Station Weddell panel, $\alpha = 0.060$ and $F = 3$.

Both panels in Fig. 3 probably suffer from fictitious correlation, however, because z_0 is evaluated from (6) in the form

$$z_0 = r \exp \left\{ - \left[\frac{kS_r}{u_*} + \psi_m(\zeta) \right] \right\}. \tag{9}$$

That is, in Fig. 3, the measured u_* appears prominently in both the dependent and independent variables. (Note that ζ also includes u_* .)

In the literature, the data for z_0 - u_* plots often derive from measurements of the wind speed profile $U(z)$, where z is the measurement height. Because the wind speed measured in the atmospheric surface layer is presumed to obey Monin–Obukhov similarity, its profile is represented as

$$U(z) = \frac{u_*}{k} [\ln(z/z_0) - \psi_m(\zeta)]. \tag{10}$$

The stability correction ψ_m here makes using (10) to analyze data difficult unless we also have simultaneous profile measurements of potential temperature and specific humidity and can thereby iteratively solve the three profile equations for the Obukhov length. In the absence of these extra profiles, most determinations of u_* and z_0 from profile measurements require near-neutral stratification, when Eq. 10 simplifies to

$$U(z) = \frac{u_*}{k} \ln(z) - \frac{u_*}{k} \ln(z_0). \tag{11}$$

In such neutral stratification, plots of $U(z)$ versus $\ln(z)$ can be fit with a straight line such that the slope is u_*/k and the intercept (I) is $-(u_*/k)\ln(z_0)$. This analysis similarly produces fictitious correlation between z_0 and u_* because here z_0 is calculated as

$$z_0 = \exp \left(- \frac{kI}{u_*} \right). \tag{12}$$

But for any reference height r , (11) provides the relation

$$I = U_r - \frac{u_*}{k} \ln(r), \tag{13}$$

where U_r is the wind speed at height r . Consequently, with (13) inserted for I , (12) becomes

$$z_0 = r \exp \left(- \frac{kU_r}{u_*} \right), \tag{14}$$

which is similar to the expression that we obtain from eddy-covariance measurements, see Eq. 9. That is, here too, the measured u_* is embedded in z_0 .

To see what effect this shared u_* has on analyses of z_0 versus u_* , I rewrite Eq. 9 as

$$\ln(z_0) = \ln(r) - \left[\frac{kS_r}{u_*} + \psi_m(\zeta) \right] \tag{15}$$

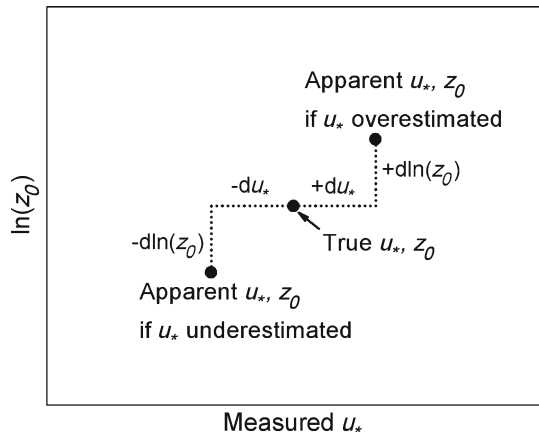
because Fig. 3 shows plots of $\ln(z_0)$ versus u_* . The dependence of $\ln(z_0)$ on the measured u_* is thus

$$\frac{\partial \ln(z_0)}{\partial u_*} = \frac{kS_r}{u_*^2} - \frac{\partial \psi_m(\zeta)}{\partial \zeta} \frac{\partial \zeta}{\partial u_*}. \tag{16}$$

From (4) and the definition $\zeta \equiv r/L$, we see that

$$\frac{\partial \zeta}{\partial u_*} = - \frac{3\zeta}{u_*}. \tag{17}$$

Fig. 4 How the fictitious correlation arises. Because the bracketed term in (21) is almost always positive, random errors in the measured u_* (denoted du_*) induce random errors in $\ln(z_0)$ [denoted $d\ln(z_0)$] with the same sign. Plots of $\ln(z_0)$ versus measured u_* thus tend to have a positive slope



Because $\psi_m(\zeta)$ derives from (e.g., Panofsky 1963)

$$\psi_m(\zeta) = \int_0^\zeta \frac{1 - \phi_m(\zeta')}{\zeta'} d\zeta', \tag{18}$$

where ϕ_m is the flux-gradient Monin–Obukhov similarity function (e.g., Paulson 1970; Grachev et al. 2007), we see, by invoking Leibniz’s rule, that

$$\frac{\partial \psi_m(\zeta)}{\partial \zeta} = \frac{1 - \phi_m(\zeta)}{\zeta}. \tag{19}$$

Equation 16, in turn, becomes

$$\frac{\partial \ln(z_0)}{\partial u_*} = \frac{kS_r}{u_*^2} + \frac{3[1 - \phi_m(\zeta)]}{u_*}. \tag{20}$$

Therefore, if a measurement of u_* has an error of du_* , the corresponding error in $\ln(z_0)$ is

$$d\ln(z_0) = \left[\frac{kS_r}{u_*^2} + \frac{3(1 - \phi_m)}{u_*} \right] du_*. \tag{21}$$

If we now plot $\ln(z_0)$ versus the measured u_* , these errors are correlated and thereby affect visual and statistical interpretations of the data.

To demonstrate the consequences of (21), I evaluated the term in square brackets for each of the u_* averaging bins in the Ice Station Weddell panel in Fig. 3. In 21 of those bins, that term is positive and has a value ranging between 14 and 130 s m^{-1} ; in only one bin is it negative. Figure 4 depicts what these results imply.

For all u_* values—not just values above the drifting snow threshold—the correlated errors in $\ln(z_0)$ and u_* cause $\ln(z_0)$ to appear to increase with u_* . Figure 4 shows that, because $kS_r/u_*^2 + 3(1 - \phi_m)/u_*$ is virtually always positive, an overestimate of u_* produces an overestimate in $\ln(z_0)$; and an underestimate of u_* produces an underestimate in $\ln(z_0)$. Plots of $\ln(z_0)$ versus measured u_* , as in Fig. 3, thus naturally tend to show $\ln(z_0)$ increasing with u_* because of the shared u_* —an effect that I term fictitious correlation (e.g., Andreas 2002, 2009; Andreas and Hicks 2002; Andreas et al. 2006).

To mitigate the misleading effects of such fictitious correlation in scatter plots such as those in Fig. 3, Andreas et al. (2006, 2010b) suggested using, in the independent variable,

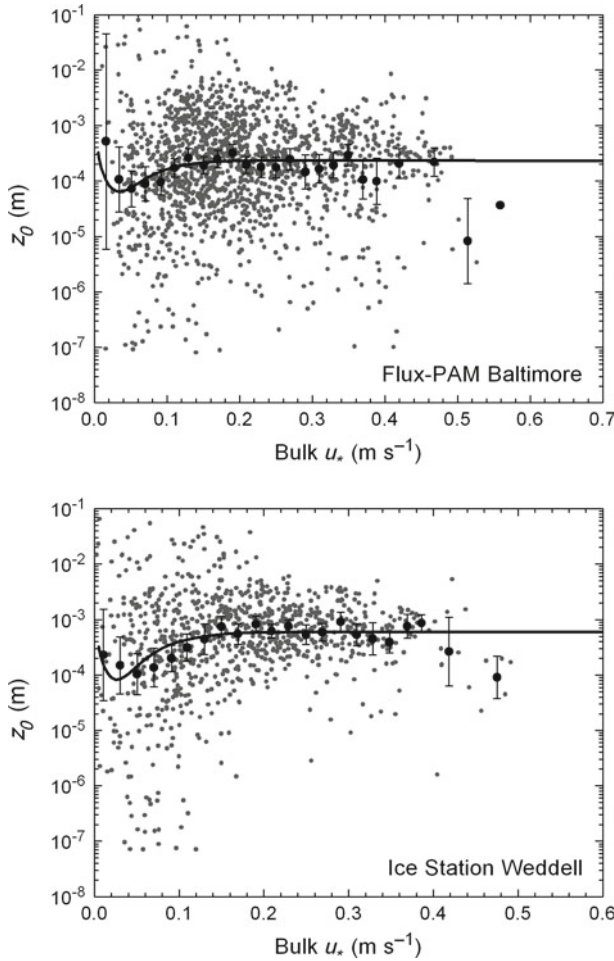


Fig. 5 The same z_0 values as in Fig. 3. Here, though, the independent variable is the u_* value from a bulk flux algorithm, $u_{*,B}$. The curves in the two panels are (22), with $B = 2.3 \times 10^{-4}$ for the Baltimore panel and with $B = 6.0 \times 10^{-4}$ for the Ice Station Weddell panel

quantities calculated from a bulk flux algorithm rather than measured quantities. In other words, as the independent variable in Fig. 3, the measured u_* is replaced with the u_* derived from a bulk flux algorithm. In fact, this is the proper approach for developing and validating bulk flux algorithms. Because of the coupling among the equations in these algorithms, the goal is to iteratively obtain an accurate estimate of z_0 , for example, that is associated with the bulk estimate of u_* .

Figure 5 demonstrates the difference that this approach makes in interpreting the behaviour of z_0 . The two panels show the same z_0 measurements as in Fig. 3; but now the independent variable is an estimate of u_* from a bulk flux algorithm (denoted $u_{*,B}$). Neither panel exhibits the dramatic decrease in z_0 with decreasing u_* that was evident in Fig. 3. And when u_* is above the range influenced by aerodynamically smooth flow (i.e., $u_{*,B} > 0.2 \text{ m s}^{-1}$), z_0 is constant: that is, it does not increase with friction velocity as was the case in Fig. 3.

Equation 21 and Fig. 4 explain the difference. Although $\ln(z_0)$ still has random errors resulting from the errors in the measured u_* , those errors are not correlated with the random errors in $u_{*,B}$. As a consequence, plots of $\ln(z_0)$ versus $u_{*,B}$ do not behave as in Fig. 3.

The increase with increasing u_* that z_0 exhibits in Fig. 3 is consequently an artifact of the shared measurements of u_* : it is fictitious correlation. For $u_{*,B}$ values below 0.6 m s^{-1} , neither the SHEBA nor Ice Station Weddell data in Fig. 5 show any evidence that drifting snow causes z_0 to increase. Four other independent datasets from SHEBA (see Fig. 2 in Andreas et al. 2010b) demonstrate this same result.

The curves in the two panels in Fig. 5 have the form

$$z_0 = 0.135 \frac{\nu}{u_{*,B}} + B \tanh^3(13u_{*,B}), \quad (22)$$

where ν is the kinematic viscosity of air in $\text{m}^2 \text{ s}^{-1}$. Equation 22 with $B = 2.3 \times 10^{-4}$ is from the SHEBA bulk flux algorithm (Andreas et al. 2010b) and is plotted in the Baltimore panel in Fig. 5. In the Ice Station Weddell panel, (22) with $B = 6.0 \times 10^{-4}$ fits the z_0 data better. I used Eq. 22 with the respective B values in the bulk flux algorithm to compute $u_{*,B}$ in the Baltimore and Ice Station Weddell panels in Fig. 5.

The most conspicuous difference between Figs. 3 and 5 is in the behaviour of z_0 for small u_* . In Fig. 3, z_0 becomes smaller as the measured u_* becomes smaller. Figure 5, in contrast, suggests that z_0 obeys aerodynamically smooth scaling for small u_* when plotted against the bulk u_* : z_0 becomes larger as $u_{*,B}$ becomes smaller for small $u_{*,B}$. The first term on the right-hand side of Eq. 22 represents this behaviour. In effect, the fictitious correlation completely obscures this known theoretical and empirical behaviour of z_0 for small u_* .

In summary, I conclude that the idea that the roughness length z_0 for drifting snow increases with u_*^2 is a fallacy that has persisted because of flawed analyses. Scatter plots of measured z_0 versus measured u_* (e.g., Fig. 3) suffer from fictitious correlation because the measured u_* is also required for calculating z_0 . Hence, errors in u_* are translated into corresponding errors in z_0 . Plots of measured z_0 against a bulk flux estimate of u_* , on the other hand (as in Fig. 5), mitigate the fictitious correlation and show no increase in z_0 with $u_{*,B}$ in the drifting snow regime, at least up to $u_{*,B}$ of 0.6 m s^{-1} .

In effect, the analysis demonstrates that snow-covered sea ice—and probably any extensive snow-covered surface—is not a mobile surface in the same sense that the ocean is; its roughness length does not increase with friction velocity for the wind speeds reported here.

6 Conclusions

Data collected over snow-covered sea ice at SHEBA and on Ice Station Weddell corroborate observations of drifting snow made over other snow-covered surfaces: the threshold friction velocity for drifting snow ($u_{*,t}$) is in the vicinity of 0.3 m s^{-1} . These drifting snow observations at SHEBA were made with a laser scintillometer. To my knowledge, this is the first reported example of using a scintillometer for detecting drifting snow.

The roughness length, z_0 , over snow-covered surfaces is often presumed to scale with the friction velocity, u_* . Measurements of z_0 are, thus, typically plotted against measurements of u_* and exhibit a Charnock-like behaviour, see Eq. 1. The implication is that snow behaves as a mobile surface such that z_0 increases as u_*^2 when snow begins drifting once u_* reaches the drifting threshold.

Data from both SHEBA and Ice Station Weddell, however, suggest that plots showing z_0 to increase with u_* suffer from fictitious correlation because the u_* measurements are

necessary for calculating z_0 (see Fig. 3). In other words, the dependent and independent variables include some of the same measurements and, thus, have built-in correlation that obscures the physics.

The proper way to compare z_0 with u_* , and the proper way to develop a bulk flux algorithm, is to plot the z_0 measurements against the u_* values estimated with a bulk flux algorithm or against another independently obtained u_* . For example, measuring the wind speed profile could yield z_0 from (12) while simultaneous eddy-covariance measurements give u_* . Or two eddy-covariance instruments could be used: one would provide u_* directly while the other gives z_0 from (6).

In such cases, when z_0 and u_* do not share the same measurements and, thus, do not have correlated errors (e.g., Fig. 5), z_0 is independent of u_* in the drifting snow region (i.e., $u_{*,B} \geq 0.3 \text{ ms}^{-1}$). I conclude, therefore, that the idea that drifting snow causes z_0 to increase with friction velocity is a fallacy perpetuated by analyses that suffered from fictitious correlation.

Acknowledgements I would like to thank my colleagues in the SHEBA Atmospheric Surface Flux Group for help in collecting, processing, and understanding the SHEBA data: Chris Fairall, Andrey Grachev, Peter Guest, Tom Horst, Rachel Jordan, and Ola Persson. I would also like to thank the other members of the meteorology team on Ice Station Weddell for help in collecting the data there: Kerry Claffey, Boris Ivanov, and Aleksandr Makshtas. Michael Lehning and an anonymous reviewer provided helpful critiques of an earlier version of this manuscript. The U.S. National Science Foundation (NSF) supported this work with awards 06-11942 and 10-19322. NSF also supported my programs on Ice Station Weddell and at SHEBA with previous awards.

References

- Andreas EL (1995) Air-ice drag coefficients in the western Weddell Sea: 2. A model based on form drag and drifting snow. *J Geophys Res* 100(C3):4833–4843
- Andreas EL (2002) Parameterizing scalar transfer over snow and ice: a review. *J Hydrometeorol* 3:417–432
- Andreas EL (2009) Relating the drag coefficient and the roughness length over the sea to the wavelength of the peak waves. *J Phys Oceanogr* 39:3011–3020
- Andreas EL (2011) Relationship between the aerodynamic and physical roughness of winter sea ice. *Q J Roy Meteorol Soc* 137:1581–1588
- Andreas EL, Claffey KJ (1995) Air-ice drag coefficients in the western Weddell Sea: 1. Values deduced from profile measurements. *J Geophys Res* 100(C3):4821–4831
- Andreas EL, Hicks BB (2002) Comments on “Critical test of the validity of Monin–Obukhov similarity during convective conditions”. *J Atmos Sci* 59:2605–2607
- Andreas EL, Fairall CW, Guest PS, Persson POG (1999) An overview of the SHEBA atmospheric surface flux program. In: Fifth conference on polar meteorology and oceanography, Dallas, TX, American Meteorological Society, pp 411–416
- Andreas EL, Fairall CW, Persson POG, Guest PS (2003) Probability distributions for the inner scale and the refractive index structure parameter and their implications for flux averaging. *J Appl Meteorol* 42:1316–1329
- Andreas EL, Jordan RE, Makshtas AP (2004) Simulations of snow, ice, and near-surface atmospheric processes on Ice Station Weddell. *J Hydrometeorol* 5:611–624
- Andreas EL, Jordan RE, Makshtas AP (2005) Parameterizing turbulent exchange over sea ice: the Ice Station Weddell results. *Boundary-Layer Meteorol* 114:439–460
- Andreas EL, Claffey KJ, Jordan RE, Fairall CW, Guest PS, Persson POG, Grachev AA (2006) Evaluations of the von Kármán constant in the atmospheric surface layer. *J Fluid Mech* 559:117–149
- Andreas EL, Persson POG, Hare JE (2008) A bulk turbulent air-sea flux algorithm for high-wind, spray conditions. *J Phys Oceanogr* 38:1581–1596
- Andreas EL, Horst TW, Grachev AA, Persson POG, Fairall CW, Guest PS, Jordan RE (2010a) Parametrizing turbulent exchange over summer sea ice and the marginal ice zone. *Q J Roy Meteorol Soc* 136:927–943

- Andreas EL, Persson POG, Jordan RE, Horst TW, Guest PS, Grachev AA, Fairall CW (2010b) Parameterizing turbulent exchange over sea ice in winter. *J Hydrometeorol* 11:87–104
- Banke EG, Smith SD, Anderson RJ (1980) Drag coefficients at AIDJEX from sonic anemometer measurements. In: Pritchard RS (ed) *Sea ice processes and models*. University of Washington Press, Seattle, pp 430–442
- Bintanja R, Van den Broeke MR (1995) Momentum and scalar transfer coefficients over aerodynamically smooth Antarctic surfaces. *Boundary-Layer Meteorol* 74:89–111
- Bonekamp H, Komen GJ, Sterl A, Janssen PAEM, Taylor PK, Yelland MJ (2002) Statistical comparisons of observed and ECMWF modeled open ocean surface drag. *J Phys Oceanogr* 32:1010–1027
- Brunke MA, Zhou M, Zeng X, Andreas EL (2006) An intercomparison of bulk aerodynamic algorithms used over sea ice with data from the Surface Heat Budget for the Arctic Ocean (SHEBA) experiment. *J Geophys Res* 111:C09001. doi:[10.1029/2005JC002907](https://doi.org/10.1029/2005JC002907)
- Chamberlain AC (1983) Roughness length of sea, sand, and snow. *Boundary-Layer Meteorol* 25:405–409
- Charnock H (1955) Wind stress on a water surface. *Q J Roy Meteorol Soc* 81:639
- Clifton A, Rüedi J-D, Lehning M (2006) Snow saltation threshold measurements in a drifting-snow wind tunnel. *J Glaciol* 52:585–596
- De Bruin HAR, Meijninger WML, Smedman A-S, Magnusson M (2002) Displaced-beam small aperture scintillometer test. Part I: the WINTEX data-set. *Boundary-Layer Meteorol* 105:129–148
- Déry SJ, Taylor PA (1996) Some aspects of the interaction of blowing snow with the atmospheric boundary layer. *Hydrol Proc* 10:1345–1358
- Doorschot JJJ, Lehning M, Vrouwe A (2004) Field measurements of snow-drift threshold and mass fluxes, and related simulations. *Boundary-Layer Meteorol* 113:347–368
- Fairall CW, Bradley EF, Rogers DP, Edson JB, Young GS (1996) Bulk parameterization of air-sea fluxes for Tropical Ocean-Global Atmosphere Coupled-Ocean Atmosphere Response Experiment. *J Geophys Res* 101(C2):3747–3764
- Fairall CW, Bradley EF, Hare JE, Grachev AA, Edson JB (2003) Bulk parameterization of air-sea fluxes: updates and verification for the COARE algorithm. *J Clim* 16:571–591
- Fuehrer PL, Friehe CA (2002) Flux corrections revisited. *Boundary-Layer Meteorol* 102:415–457
- Garratt JR (1992) *The atmospheric boundary layer*. Cambridge University Press, Cambridge, UK, 316 pp
- Grachev AA, Fairall CW, Persson POG, Andreas EL, Guest PS (2005) Stable boundary-layer scaling regimes: the SHEBA data. *Boundary-Layer Meteorol* 116:201–235
- Grachev AA, Andreas EL, Fairall CW, Guest PS, Persson POG (2007) SHEBA flux–profile relationships in the stable atmospheric boundary layer. *Boundary-Layer Meteorol* 124:315–333
- Guest PS, Davidson KL (1991) The aerodynamic roughness of different types of sea ice. *J Geophys Res* 96(C3):4709–4721
- Horst TW, Oncley SP, Semmer SR (1997) Measurement of water vapor fluxes using capacitance RH sensors and cospectral similarity. In: Twelfth symposium on boundary layers and turbulence, Vancouver, BC, American Meteorological Society, pp 360–361
- Joffre SM (1982) Momentum and heat transfers in the surface layer over a frozen sea. *Boundary-Layer Meteorol* 24:211–229
- Johnson HK, Højstrup J, Vested HJ, Larsen SE (1998) On the dependence of sea surface roughness on wind waves. *J Phys Oceanogr* 28:1702–1716
- Kind RJ (1976) A critical examination of the requirements for model simulation of wind-induced erosion/deposition phenomena such as drifting snow. *Atmos Environ* 10:219–227
- King JC, Pomeroy JW, Gray DM, Fierz C (2008) The fluxes involved in the energy balance. In: Armstrong RL, Brun E (eds) *Snow and climate: physical processes, surface energy exchange and modeling*. Cambridge University Press, Cambridge, UK, pp 73–83
- König G (1985) Roughness length of an Antarctic ice sheet. *Polarforschung* 55:27–32
- Liston GE, Sturm M (1998) A snow-transport model for complex terrain. *J Glaciol* 44:498–516
- Male DH (1980) The seasonal snow cover. In: Colbeck SC (ed) *Dynamics of snow and ice masses*. Academic Press, New York, pp 305–395
- Mann GW, Anderson PS, Mobbs SD (2000) Profile measurements of blowing snow at Halley, Antarctica. *J Geophys Res* 105(D19):24,491–24,508
- Militzer JM, Michaelis MC, Semmer SR, Norris KS, Horst TW, Oncley SP, Delany AC, Brock FV (1995) Development of the prototype PAM III/Flux-PAM surface meteorological station. In: Ninth symposium on meteorological observations and instrumentation, Charlotte, NC, American Meteorological Society, pp 490–494
- Overland JE (1985) Atmospheric boundary layer structure and drag coefficients over sea ice. *J Geophys Res* 90(C5):9029–9049
- Owen PR (1964) Saltation of uniform grains in air. *J Fluid Mech* 20:225–242

- Panofsky HA (1963) Determination of stress from wind and temperature measurements. *Q J Roy Meteorol Soc* 89:85–94
- Paulson CA (1970) The mathematical representation of wind speed and temperature profiles in the unstable atmospheric surface layer. *J Appl Meteorol* 9:857–861
- Persson POG, Fairall CW, Andreas EL, Guest PS, Perovich DK (2002) Measurements near the Atmospheric Surface Flux Group tower at SHEBA: near-surface conditions and surface energy budget. *J Geophys Res* 107:8045. doi:10.1029/2000JC000705
- Pomeroy JW, Gray DM (1990) Saltation of snow. *Water Resour Res* 26:1583–1594
- Pomeroy JW, Gray DM, Landine PG (1993) The prairie blowing snow model: characteristics, validation, operation. *J Hydrol* 144:165–192
- Radok U (1968) Deposition and erosion of snow by the wind. Res. Rep. 230, U.S. Army Cold Regions Research and Engineering Laboratory, Hanover, NH, 23 pp
- Raupach MR (1991) Saltation layers, vegetation canopies and roughness lengths. *Acta Mech (Suppl)* 1:83–96
- Schmidt RA (1986) Transport rate of drifting snow and the mean wind speed profile. *Boundary-Layer Meteorol* 34:213–241
- Smith SD (1988) Coefficients for sea surface wind stress, heat flux, and wind profiles as a function of wind speed and temperature. *J Geophys Res* 93(C12): 15,467–15,472
- Tabler RD (1980) Self-similarity of wind profiles in blowing snow allows outdoor modeling. *J Glaciol* 26: 421–434
- Uttal T, Curry JA, McPhee MG, Perovich DK, Moritz RE, Maslanik JA, Guest PS, Stern HL, Moore JA, Turenne R, Heiberg A, Serreze MC, Wylie DP, Persson OG, Paulson CA, Halle C, Morison JH, Wheeler PA, Makshtas A, Welch H, Shupe MD, Intrieri JM, Stamnes K, Lindsey RW, Pinkel R, Pegau WS, Stanton TP, Grenfeld TC (2002) Surface Heat Budget of the Arctic Ocean. *Bull Am Meteorol Soc* 83:255–275
- Webb EK, Pearman GI, Leuning R (1980) Correction of flux measurements for density effects due to heat and water vapour transfer. *Q J Roy Meteorol Soc* 106:85–100
- Wieringa J (1993) Representative roughness parameters for homogeneous terrain. *Boundary-Layer Meteorol* 63:323–363
- Wyngaard JC (2010) *Turbulence in the atmosphere*. Cambridge University Press, Cambridge, UK, 393 pp